Contents lists available at ScienceDirect

Arabian Journal of Chemistry

journal homepage: www.ksu.edu.sa

Constructing AgI/BiSI p-n heterojunctions with an internal electric field for efficient degradation of refractory organic pollutants

Jin Liu [a,*], Qian Zhong [a], Yanjin Wang [a], Zezhi Zhang [a], Huiqin Zheng [a,*], Bin Yan [b], Yurong Shi [b]

[a] College of Environmental Economics, Henan Finance University, Zhengzhou 450046, China
[b] School of Materials Science and Engineering, North China University of Water Resources and Electric Power, Zhengzhou, 450000, China

ARTICLE INFO

Keywords:
Photocatalytic
P-n heterojunction
AgI/BiSI
Pollutant degradation

ABSTRACT

Designing photocatalysts with p-n heterojunction structures is an effective way to boost the separation of photogenerated carriers and stimulate the photocatalytic degradation activity. Herein, an efficient visible-light responsive AgI/BiSI p-n heterojunction photocatalyst was successfully constructed. X-ray photoelectron spectroscopy (XPS), photoluminescence (PL) spectroscopy, and electrochemical measurements confirmed that the AgI/BiSI p-n heterojunction structure was beneficial to the separation and transfer of photogenerated carriers, promoting the generation of main active species ($\bullet O_2^-$ and h^+). Furthermore, the photocatalytic degradation rate constants of Acid Red 1 (0.4699 min^{-1}) and metronidazole (0.0730 min^{-1}) over the optimal AgI/BiSI were about 8.4 and 3.0 times higher than those over pure AgI, respectively. This work provides a heterojunction engineering strategy to design high-efficient photocatalysts for the degradation of refractory organic pollutants.

1. Introduction

With the rapid development of urbanization and industrialization, environmental damage and energy shortage have become global issues. Among them, water environmental contaminated by organic dyes and antibiotics has attracted extensive concern. Azo dyes are one of the largest-group of colorants used in the textile and papermaking industries, which are characterized by the presence of one or more azo bonds (–N = N–). These colored azo dyes can be converted into carcinogen aromatic amines by hydrolysis, photolysis, and chemical oxidation in the natural ecosystem (Khosroshahi and Mehrizad, 2019). Metronidazole (MNZ), a typical nitroimidazole antibiotic, is widely used in the treatment of human gingival and respiratory tract infections. However, it is difficult to degrade and can be enriched in water, which is potentially carcinogenic to humans, and easily leads to the production of multidrug-resistant bacteria (Sudhir Ekande and Kumar, 2021; Wu et al., 2022).

Owing to the stable molecular structures, low solubility, and high toxicity, these organics are difficult to be eliminated by traditional microbial methods (Zhang et al., 2023; Tan et al., 2023; Podurets et al., 2022; Ming et al., 2021). As a typical advanced oxidation process, semiconductor photocatalysis exhibits significant advantages in removing organic pollutants due to the generation of active radicals with strong oxidation ability, non-secondary pollution, and potential utilization of solar energy (Ju et al., 2024; Wang et al., 2024; Li et al., 2023; Zheng et al., 2021; Lu et al., 2013). Although photocatalysis has made great progress in recent years, its reaction efficiency and visible light utilization are still far from the needs of wastewater treatment. To overcome these crucial challenges, it is necessary to explore efficient photocatalysts. Meanwhile, some strategies, such as element doping, facet engineering, vacancy engineering and heterojunction construction, were used to modify photocatalysts to expand light absorption range, and accelerate charge separation and transfer (Liu et al., 2024; Yang et al., 2022; Li et al., 2020; Ma et al., 2019; Zheng et al., 2021; Atuchin et al., 2019; Yuan et al., 2024).

BiSI as a common class of Bi^{III}-VI^{A}-VII^{A} materials received extensive attention due to its piezoelectric, pyroelectric, and photoelectric properties (Quarta et al., 2023; Quarta et al., 2022; Ganose et al., 2018; Ran et al., 2018; Moroz and Prokhorenko, 2016). As a photocatalyst, the bandgap value of BiSI is less than 1.6 eV (Ganose et al., 2016), indicating its potential visible light absorption capacity. However, rapid recombination of photogenerated electron-hole pairs seriously limits the photocatalytic activity of BiSI. Various methods have been used to address this shortcoming, such as element doping and heterojunction construction. For instance, Liu et al. (Liu et al., 2022) confirmed that doping oxygen in BiSI nanorods facilitated the Cr(VI) adsorption, light

* Corresponding authors.
E-mail addresses: liuzejin1026@126.com (J. Liu), zhenghuiqin2000@163.com (H. Zheng).

https://doi.org/10.1016/j.arabjc.2024.105844
Received 21 February 2024; Accepted 21 May 2024
Available online 23 May 2024

absorption, and charge transfer, thus promoting photocatalytic reduction of Cr(VI). Cao et al. reported that g-C_3N_4-BiSI n-n heterojunctions exhibited enhanced photocatalytic performances towards the fixation of N_2 and degradation of MB and phenol under visible light irradiation, which was attributed to the efficient transfer and separation of charge carriers.

In recent years, the construction of p-n heterojunction is a classical strategy to improve the catalytic activity of photocatalysts (Lu et al., 2022). Compared with the single semiconductor photocatalyst, the p-n heterojunction photocatalysts showed strong redox ability, broad spectrum adsorption. In addition, the heterojunction between p-type and n-type semiconductors could accelerate the charge carrier separation by forming an internal electric field, thereby improving photocatalytic performances. As a p-type semiconductor, AgI is often used to modify n-type semiconductors, such as α-MnO_2 (Salari and Kohantorabi, 2020), $BiVO_4$ (Zhao et al., 2019) and $Bi_2O_2CO_3$ (Zhang et al., 2017), to prepare p-n heterojunction photocatalysts. In this work, AgI/BiSI p-n heterojunction photocatalysts were successfully synthesized via a facile deposition process. Compared with the AgI and BiSI, the AgI/BiSI p-n heterojunction exhibited enhanced visible-light photocatalytic performances for the degradation of Acid Red 1 (AR1, a typical azo dye) and antibiotic MNZ. Furthermore, the charge transfer process of AgI/BiSI p-n heterojunction and degradation mechanism were investigated. This work could provide a new insight to develop high-efficiency visible-light photocatalysts for organic wastewater treatment.

2. Experimental section

2.1. Chemicals

Bismuth Chloride ($BiCl_3$), thiourea $(NH_2)_2CS$), sodium iodide (NaI), silver nitrate ($AgNO_3$), potassium iodide (KI), ethanol (C_2H_5OH), 5,5-dimethyl-1-pyrroline-N-oxide (DMPO), and 2,2,6,6-Tetramethylpiperidinooxy (TEMPO) were purchased from Aladdin Industrial Corporation (Shanghai, China). All the reagents were of analytical grade, and they were used without additional purification.

2.2. Synthesis of BiSI nanorod photocatalysts

BiSI nanorod photocatalysts were prepared by a solvothermal method described previously (Liu et al., 2022). Typically, 2 mmol of $BiCl_3$, 2 mmol of $(NH_2)_2CS$, and 8 mmol of NaI were dissolved into 60 mL of C_2H_5OH under magnetic stirring. Afterwards, the mixture was sealed in a Teflon-lined stainless steel autoclave (100 mL) and treated at 140 °C for 24 h. Subsequently, the black sediment was washed and dried at 60 °C for 12 h.

2.3. Synthesis of AgI/BiSI photocatalysts

AgI/BiSI photocatalysts were synthesized via a facile deposition process. Briefly, 0.3 g of as-prepared BiSI photocatalyst was ultrasonically dispersed in 100 mL of deionized water for 1 h at room temperature. After that, KI with the desired amount was added into the suspension and stirred for 1 h in the dark. Then, 20 mL of aqueous solution containing the corresponding amount of $AgNO_3$ was added dropwise into the above suspension under vigorous stirring, and the resulting suspension was stirred for another 1 h. Finally, the AgI/BiSI photocatalysts were collected by centrifugation, washed with deionized water and dried at 60 °C for 12 h. The AgI/BiSI photocatalysts with different mass fractions of AgI (10 %, 20 %, 30 %, and 40 %) were recorded as 1AgI/BiSI, 2AgI/BiSI, 3AgI/BiSI, and 4AgI/BiSI, respectively. For comparison, pure AgI was also prepared by the same procedure without adding BiSI nanorods.

2.4. Characterization

An D8 X-ray diffractometer (XRD, Bruker) and an X-ray photoelectron spectrometer (XPS, Thermo Fisher) were employed to identify the phase/chemical composition and constituent element valence states of the catalysts. The morphology of samples was recorded by scanning electron microscope (SEM, FEI Quanta 200) and transmission electron microscope (TEM, Hitachi HT7800). Electron spin resonance (ESR) spectra were collected on a Bruker A300 spectrometer. The photoluminescence (PL) spectra were recorded by a FLS1000 fluorescence spectrophotometer. UV–visible diffuse reflectance spectra (UV–Vis DRS) were measured by a spectrophotometer (UV-2600, Shimadzu). Photoelectrochemical tests were performed with a Chenhua electrochemical workstation (CHI660E). The electrical conductivity types of samples were identified by the Hall Effect measurements (Lakeshore 8400, USA) at room temperature.

2.5. Photocatalytic experiments

The photocatalytic activities of photocatalysts were evaluated by degrading the AR1 dye and MNZ antibiotic. The temperature of pollutant solution was maintained at 20 °C throughout the photocatalytic experiments by a circulating cooling water system. Typically, 0.05 g of photocatalyst was added in a 200 mL double-walled glass reactor with 100 mL solution (30 mg/L AR1 or 10 mg/L MNZ). Afterwards, the suspension was stirred in the dark for 30 min and then irradiated by a 100 W LED light source with a wavelength of 420 nm (PLS-LED100C, Beijing Perfectlight). During the degradation process, about 3 mL of suspension sample was collected at regular time intervals, and then filtered with 0.45 μm membrane. The concentration of residual AR1 and MNZ was monitored by the spectrophotometer (UV-2600, Shimadzu) at their characteristic band of 531 and 320 nm, respectively.

3. Results and discussion

3.1. Composition and structure characteristics

As shown in Fig. 1a, XRD patterns of AgI and BiSI samples are consistent with the standard XRD patterns of hexagonal AgI (JCPDS No. 09–0374) and orthorhombic BiSI (JCPDS No. 43–0652) references (Sun et al., 2021; Wang et al., 2021), respectively. All AgI/BiSI composites exhibited the characteristic peaks of AgI and BiSI. The peaks of AgI in the AgI/BiSI composites became stronger with the increase of AgI content, and it confirmed the increasing content of AgI in the composites. Meanwhile, XPS measurements were also employed to analyze the composition and charge transfer of AgI/BiSI composites. The XPS survey spectra confirmed the presence of Ag, I, Bi and S elements in the AgI/BiSI composites (Fig. 1b), which agreed well with the XRD results. Compared with the AgI, the Ag 3d XPS peaks of AgI/BiSI composite shifted to lower binding energies (Fig. 1c) (Atuchin et al., 2007). As for the Bi 4f and S 2p XPS spectra, the peak positions of AgI/BiSI composite shifted to higher binding energies than that of BiSI (Fig. 1d) (Atuchin et al., 2010; Atuchin et al., 2011). These results indicated that a strong interface interaction between BiSI and AgI, and the electrons from BiSI could transfer to AgI in the dark, suggesting the formation of a AgI/BiSI heterojunction (Wu and Song, 2023; Li et al., 2021). Therefore, the negative and positive charges could be accumulated in the AgI and BiSI, respectively (Wang et al., 2022). The redistribution of charges would be beneficial to the separation of photogenerated carriers and the improvement of photocatalytic performances (Zhang et al., 2023). In addition, the Hall effect measurements were adopted to determine the electrical conduction types of AgI and BiSI samples. In Table S1, it can be seen that that the AgI and BiSI samples exhibit p-type and n-type conductivities, respectively, which is consistent with the reported results (Quarta et al., 2022; Liu et al., 2020).

The morphology features of BiSI, AgI and 3AgI/BiSI composites were

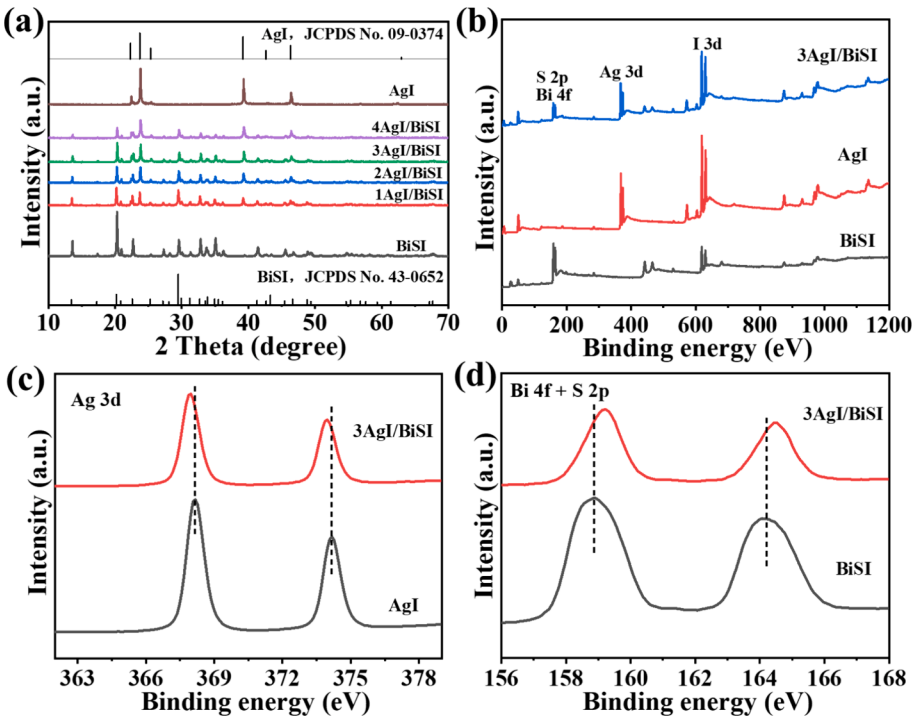

Fig. 1. (a) XRD patterns of AgI, BiSI, and AgI/BiSI composites. (b-d) XPS spectra of AgI, BiSI, and 3AgI/BiSI: (b) Survey, (c) Ag 3d, (d) Bi 4f and S 2p.

displayed by SEM images. As seen in Fig. 2a-b, the BiSI sample presented an ultralong rodlike structure and relatively smooth surface. From Fig. 2c, it can be found that the AgI sample was composed of nanoparticles. As for the SEM image of 3AgI/BiSI (Fig. 2d), a large number of AgI nanoparticles were tightly attached to the surface of rodlike BiSI. Based on the above analysis results, it was predicted that the AgI/BiSI p-n heterojunction was successfully constructed.

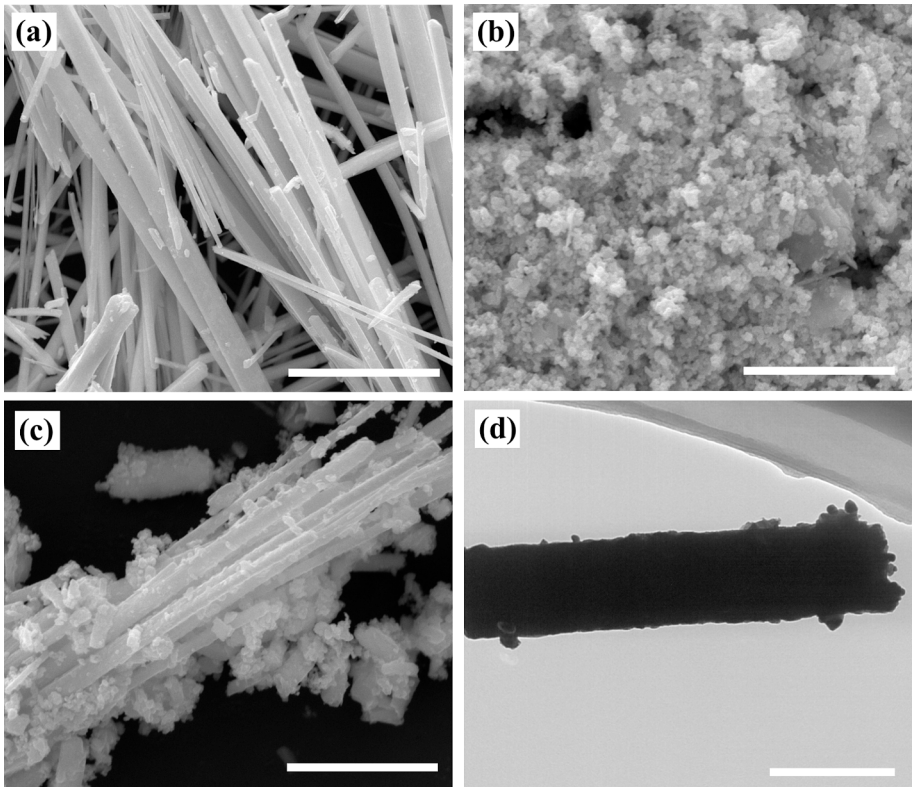

Fig. 2. SEM images of (a) BiSI (scale bar = 10 μm), (b) AgI (scale bar = 5 μm), and (c) 3AgI/BiSI (scale bar = 5 μm). (d) A TEM image of (d) 3AgI/BiSI (scale bar = 500 nm).

3.2. Optical and electrochemical properties

The optical property and energy band structure of samples were investigated by UV–Vis DRS and valence band XPS (VB-XPS) analyses. As presented in Fig. 3a, the AgI, BiSI, and 3AgI/BiSI samples exhibited strong absorption of visible light. Additionally, the band gaps (E_g) of AgI and BiSI were determined by the plotting of $(\alpha h\nu)^{2/n}$ versus photon energy ($h\nu$) (Fig. 3b-c). For direct transition AgI and indirect transition BiSI (Audzijonis et al., 2010; Zhou et al., 2021; Jatav et al., 2021; Zhou et al., 2019), n is 1 and 4, respectively. Consequently, the E_g values of the AgI and BiSI were calculated to be 2.65 and 1.39 eV, respectively. As displayed in Fig. 3d-e, the VB potentials ($E_{VB\text{-}XPS}$) of AgI and BiSI were estimated to be 1.16 and 0.92 eV vs. vacuum level, respectively. The VB potential of normal hydrogen electrode ($E_{VB\text{-}NHE}$, pH = 7) could be calculated according to the Eq. (1) (Zhang et al., 2021):

$$E_{VB-NHE} = \Phi + E_{VB-XPS} - 4.44 \quad (1)$$

where Φ is the work function (4.35 eV) of the XPS analyzer. Therefore, the $E_{VB\text{-}NHE}$ of AgI and BiSI was calculated to be 1.07 and 0.83 eV, respectively. Combined with the obtained E_g values estimated by DRS spectra, the conduction band potentials (E_{CB}) of AgI and BiSI were calculated to be −1.58 and −0.56 eV, respectively.

To unveil the charge transfer mechanism, PL spectroscopy and electrochemical measurements were performed. Initially, the PL spectra of AgI, BiSI, and 3AgI/BiSI samples were monitored under the excitation of 400 nm. From Fig. 4a, it can be found that three samples had an obvious emission peak at about 590 nm. Compared with BiSI and AgI, 3AgI/BiSI had a lower PL intensity, indicating its high charge separation efficiency (Lu et al., 2023). Electrochemical impedance spectroscopy (EIS) displays that the 3AgI/BiSI possessed a smallest arc radius (Fig. 4b), implying a least charge transfer resistance, which was in favor of reducing the electrochemical impedance of electrons and accelerating charge transfer from catalyst to solid/liquid interface (Zhong et al., 2021). Moreover, the photocurrent density of 3AgI/BiSI was much higher than that of BiSI and AgI under visible light irradiation (Fig. 4c). These results suggested that the construction of p-n heterojunction in the AgI/BiSI composite could efficiently boost the separation and transfer of photogenerated carriers.

3.3. Photocatalytic activity

To evaluate the photocatalytic performances of samples, AR1 and

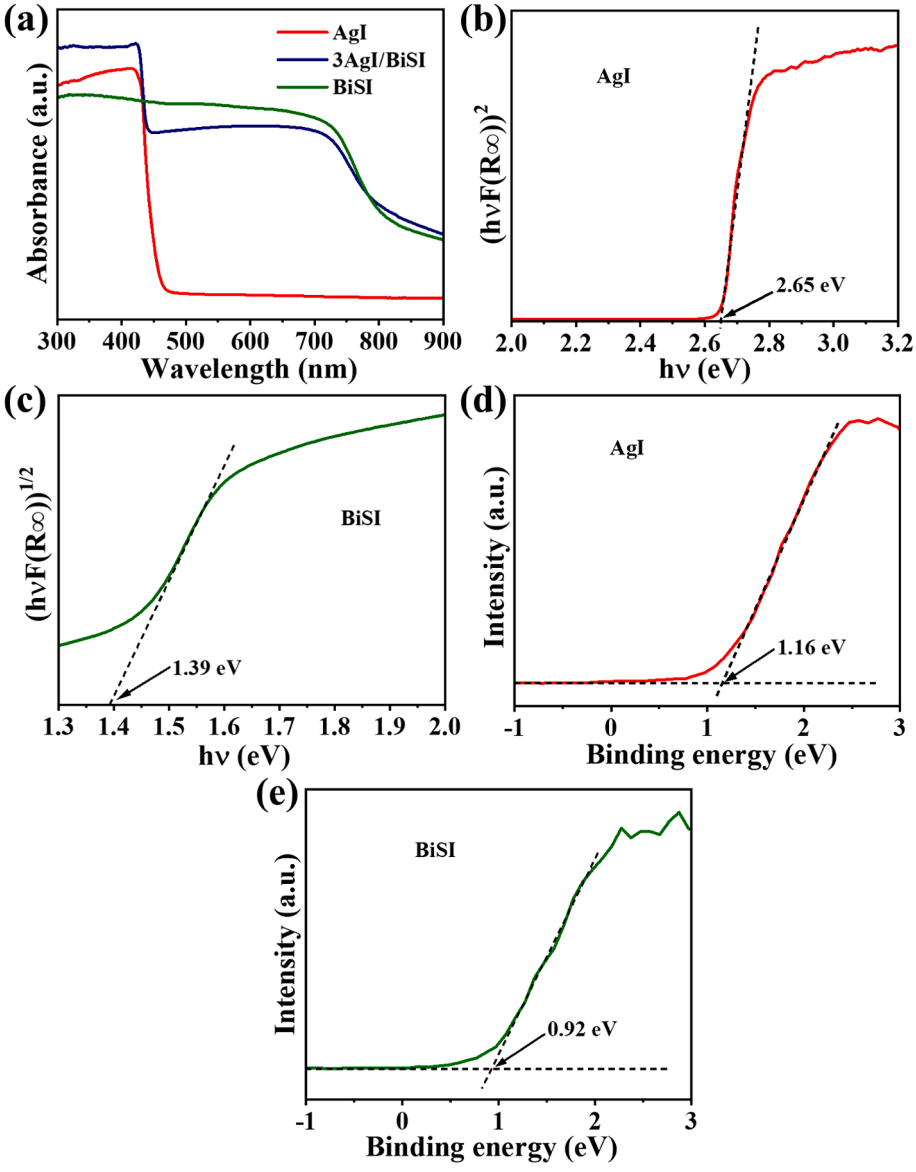

Fig. 3. (a) UV–Vis DRS of AgI, BiSI, and 3AgI/BiSI. (b, c) Band gaps and (d, e) VB-XPS spectra of AgI and BiSI.

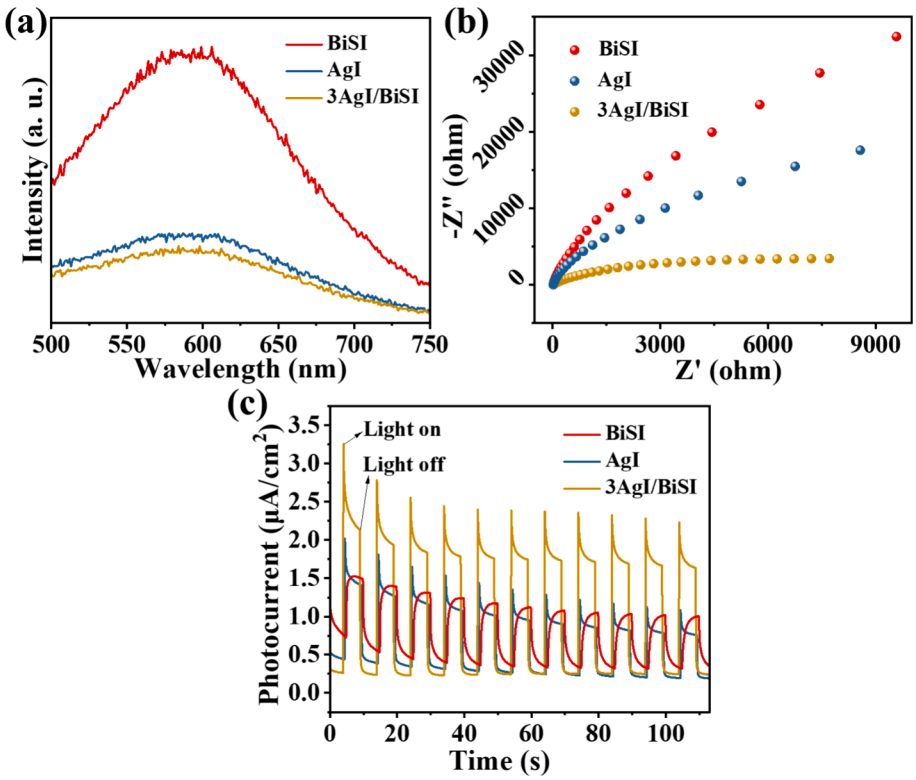

Fig. 4. (a) PL spectra, (b) EIS plots, and (c) photocurrent density of AgI, BiSI, and 3AgI/BiSI.

MNZ were used as simulated target pollutants. Fig. 5a shows the photocatalytic performances of AgI, BiSI, and AgI/BiSI samples. Compared with the single AgI and BiSI, all AgI/BiSI composites exhibited an enhanced photocatalytic activity for the degradation of AR1, which was mainly attributed to the formation of AgI/BiSI p-n heterojunctions. The optimized 3AgI/BiSI possessed a highest degradation efficiency and about 100 % of AR1 was removed after 10 min of visible light irradiation. Furthermore, it can be seen that the degradation rate of AR1 over AgI/BiSI increased when the content of AgI was modified from 10 % to 30 %. However, the degradation rate of AR1 over AgI/BiSI decreased slightly when the content of AgI was further increased to 40 %. The phenomenon was due to the excess AgI covering the surface of BiSI in the AgI/BiSI, which hindered the visible light adsorption of BiSI and ultimately reduced the photocatalytic activity (Huang et al., 2020; Dong et al., 2023). In order to unveil the degradation kinetics, the $\ln(C_0/C_t)$ vs photocatalytic reaction time was plotted (Lu et al., 2022). As shown in Fig. 5b, the photocatalytic degradation process of AR1 is well fitted by the pseudo-first-order kinetics model. The degradation rate constant (k) of AR1 for 3AgI/BiSI was calculated to be 0.4699 min^{-1}, which was about 8.4 and 70.1 times higher than that of AgI (0.0560 min^{-1}) and BiSI (0.0067 min^{-1}), respectively. Compared with the other recently reported photocatalysts, 3AgI/BiSI exhibited an obvious superiority in the photocatalytic degradation of AR1 (Table S2). Total organic carbon (TOC) was employed to evaluate the mineralization rate of organic pollutants. The mineralization rate of AR1 calculated by total organic carbon was about 29.8 % (Fig. S1). In addition, the 3AgI/BiSI could effectively photodegrade the MNZ (Fig. 5c), and its corresponding degradation rate constant was calculated to be 0.0730 min^{-1}, which was about 3.0 and 91.2 times higher than that of AgI (0.0246 min^{-1}) and BiSI (0.0008 min^{-1}) (Fig. 5d), respectively. The effect of AR1 concentration and pH values on the degradation performances of 3AgI/BiSI was also investigated and the results were shown in Fig. S2.

Generally, the reusability of photocatalysts is a key factor for their potential practical application. So, the recycling experiments for visible-light photocatalytic degradation of AR1 over 3AgI/BiSI were carried out under consistent reaction conditions, and the results are given in Fig. 6a. After each degradation experiment, the recycled 3AgI/BiSI was carefully collected, washed, and dried at 70 °C for 6 h before entering the next cycle. Obviously, the photocatalytic performance of 3AgI/BiSI was hardly lost even after 5 cycles of AR1 degradation. In Fig. 6b, it is clearly seen that the XRD patterns of original and recycled 3AgI/BiSI samples are very similar, further demonstrating the high photocatalytic stability of 3AgI/BiSI.

3.4. Mechanism discussion

To explore active species in the photocatalytic degradation process, various trapping experiments were carried out. 1,4-benzoquinone (BQ), $Na_2C_2O_4$, and isopropyl alcohol (IPA) acted as the scavengers of $\bullet O_2^-$, h^+, and •OH (Wu et al., 2021; Zhang et al., 2023; Zhou et al., 2024), respectively. Fig. 7a shows that the IPA had a negligible effect on the photocatalytic degradation of AR1, suggesting that •OH was not the dominant active species. In contrast, the degradation rate was obviously inhabited in the presence of BQ and $Na_2C_2O_4$, confirming that $\bullet O_2^-$ and h^+ had an important influence on the AR1 degradation. Moreover, the concentration of $\bullet O_2^-$ was quantitatively determined with nitroblue tetrazolium (NBT) scavengers (Wang et al., 2019). As shown in Fig. 7b, 3AgI/BiSI produced a much higher $\bullet O_2^-$ concentration than that of BiSI and AgI, which was ascribed to the p-n heterojunction structure and excellent charge transfer efficiency. To further confirm the types of reactive species, ESR measurements was performed. As shown in Fig. 7c, there was no characteristic signal of DMPO-$\bullet O_2^-$ spin-adduct was detected in the 3AgI/BiSI system in the dark. With visible light irradiation, the DMPO-$\bullet O_2^-$ signal appeared. Furthermore, the triple signals of TEMPO in Fig. 7d weakened, this was because h^+ consumed part of TEMPO (Liu et al., 2024). These findings indicated the generation of $\bullet O_2^-$ and h^+ in the 3AgI/BiSI/visible-light system.

Based on the above analyses, a possible mechanism of AgI/BiSI p-n heterojunction photocatalysts for photocatalytic degradation of organic pollutants was proposed (Fig. 8). Generally, the Fermi levels (E_f) of p-

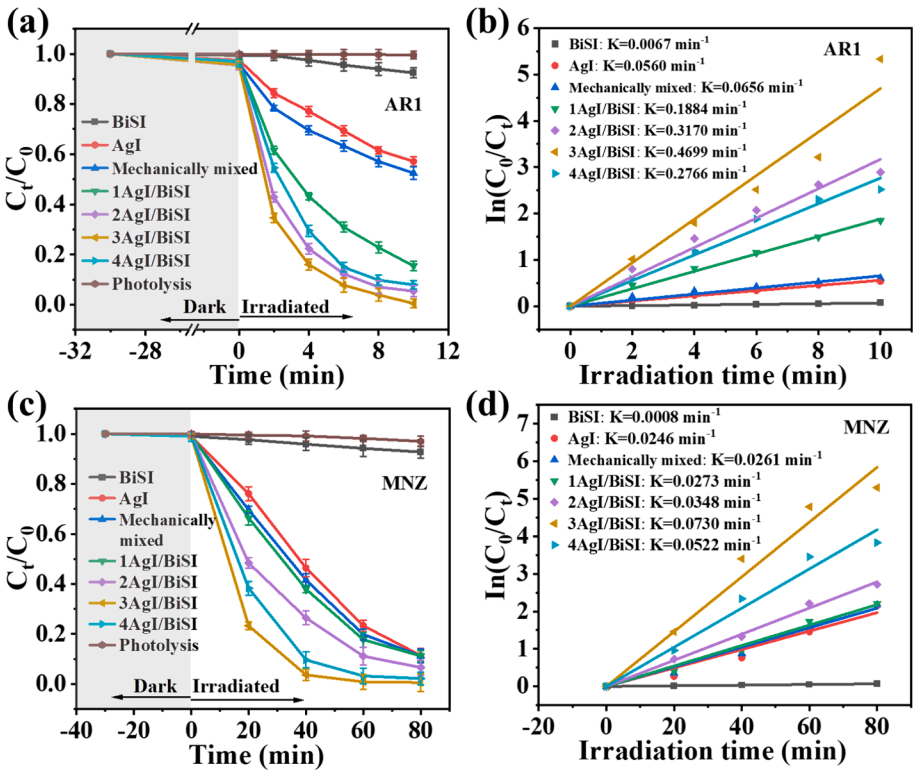

Fig. 5. Photocatalytic degradation of (a) AR1 and (c) MNZ over different photocatalysts under visible light irradiation and corresponding kinetics plots for the degradation of (b) AR1 and (d) MNZ.

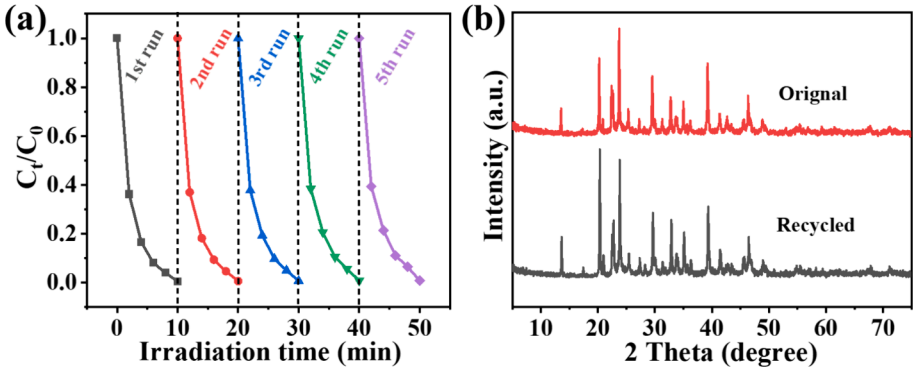

Fig. 6. Recycling experiments for the degradation of AR1 over 3AgI/BiSI. (b) XRD patterns of original and recycled 3AgI/BiSI samples.

type and n-type semiconductors are located near the conduction band (CB) and valence band (VB) (Guo et al., 2020), respectively. When p-type AgI and n-type BiSI contacted each other, charge redistribution and band bending occur at the interface, and equilibration Fermi levels were finally obtained. In the meantime, an internal electric field pointing from BiSI to AgI was created (Li et al., 2014). Under visible light irradiation, both AgI and BiSI were excited to generate electrons and holes pairs. Owing to the action of the internal electric field, the photogenerated electrons in the CB of AgI could easily transfer to the CB of BiSI, and the migration of holes in the VB of AgI and BiSI could take place in the opposite direction, which led to an efficient separation of photogenerated electron/hole pairs. Subsequently, the electrons in the CB of BiSI would reduce the dissolved oxygen to $\bullet O_2^-$. Lastly, the formed $\bullet O_2^-$ and h^+ participated in the degradation of AR1 and MNZ.

4. Conclusions

In summary, a novel AgI/BiSI p-n heterojunction photocatalyst was successfully fabricated by a facile deposition of AgI on the BiSI surface. The AgI/BiSI exhibited much higher photocatalytic performances for the degradation of AR1 and MNZ than AgI and BiSI, which could be attributed to the function of p-n heterojunctions. Moreover, the AgI/BiSI showed good stability even after recycling 5 times. $\bullet O_2^-$ and h^+ were identified as the dominant active species in the degradation process via trapping experiments and ESR spectroscopy. Photoelectrochemical analyses confirmed that the construction of p-n heterojunction in the AgI/BiSI could effectively boost the separation and transfer of photogenerated carriers, and a possible visible-light photocatalytic mechanism for pollutant degradation was proposed. This work could provide a useful insight into the design of p-n heterojunction photocatalysts for efficient degradation of refractory organic pollutants.

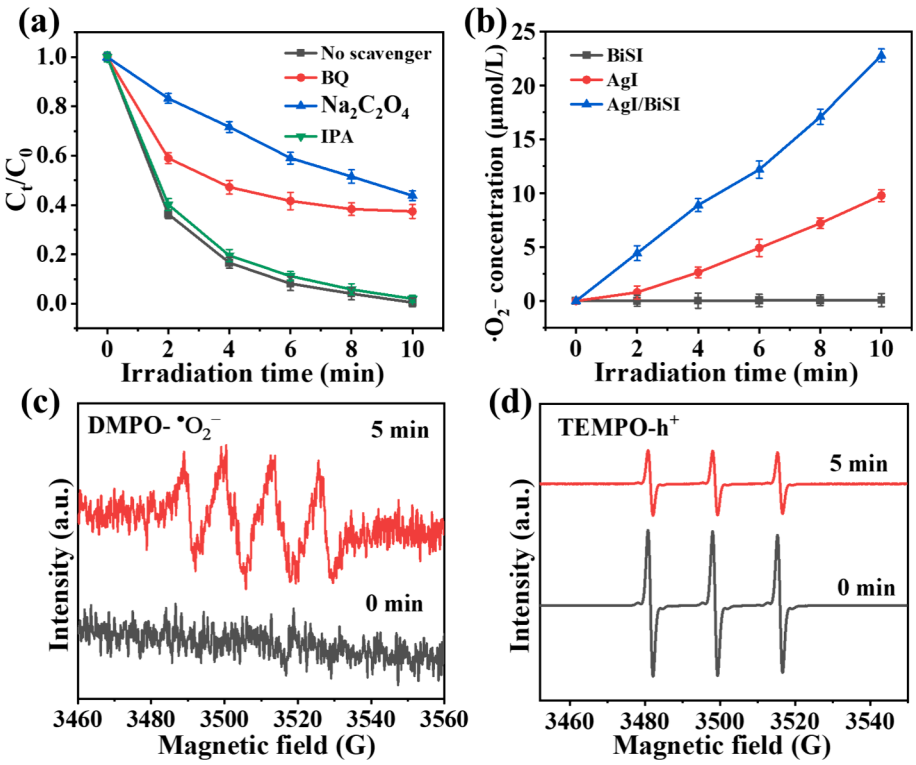

Fig. 7. (a) Photocatalytic degradation of AR1 over 3AgI/BiSI with and without scavengers. (b) The concentration of $\bullet O_2^-$ produced over AgI, BiSI, and 3AgI/BiSI. ESR spectra of (c) DMPO-$\bullet O_2^-$ and (d) TEMPO-h^+ in the 3AgI/BiSI system.

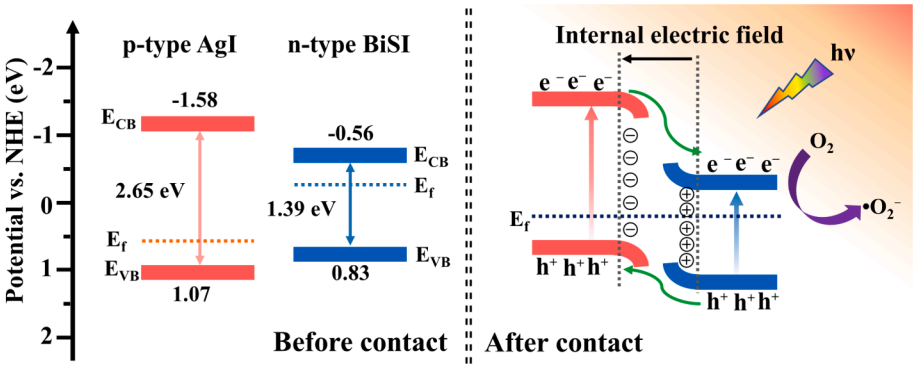

Fig. 8. Schematic band structures and charge transfer processes of AgI/BiSI p-n heterojunction photocatalysts under visible light irradiation.

5. Author agreement

All authors have seen and approved the final version of the manuscript being submitted. They warrant that the article is the authors' original work, hasn't received prior publication and isn't under consideration for publication elsewhere.

CRediT authorship contribution statement

Jin Liu: Conceptualization, Data curation, Funding acquisition, Supervision, Writing – original draft. **Qian Zhong:** Data curation, Investigation, Writing – review & editing, Writing – original draft. **Yanjin Wang:** Data curation, Formal analysis. **Zezhi Zhang:** Project administration, Supervision. **Huiqin Zheng:** Conceptualization, Formal analysis, Supervision. **Bin Yan:** Data curation, Formal analysis, Investigation. **Yurong Shi:** Data curation, Investigation, Formal analysis.

Declaration of competing interest

The authors declare that they have no known competing financial interests or personal relationships that could have appeared to influence the work reported in this paper.

Acknowledgments

This work was financially supported by the National Natural Science Foundation of China (No. 21806194), Science and Technology Project of Henan Province (No. 242102320096), Natural Science Foundation of Henan Province (No. 242300420539), and Scientific Research Start-up Foundation of Henan Finance University (No. 2024BS012).

Appendix A. Supplementary data

Supplementary data to this article can be found online at https://doi.org/10.1016/j.arabjc.2024.105844.

References

Atuchin, V.V., Kesler, V.G., Parasyuk, O.V., 2007. Electronic structure of $AgCd_2GaS_4$. Surf. Rev. Lett. 14, 403–409. https://doi.org/10.1142/s0218625x07009608.

Atuchin, V.V., Isaenko, L.I., Kesler, V.G., Lobanov, S.I., 2010. Core level photoelectron spectroscopy of $LiGaS_2$ and Ga-S bonding in complex sulfides. J. Alloys Compd. 497, 244–248. https://doi.org/10.1016/j.jallcom.2010.03.020.

Atuchin, V.V., Golyashov, V.A., Kokh, K.A., Korolkov, I.V., Kozhukhov, A.S., Kruchinin, V.N., Makarenko, S.V., Pokrovsky, L.D., Prosvirin, I.P., Romanyuk, K.N., Tereshchenko, O.E., 2011. Formation of inert Bi_2Se_3(0001) cleaved surface. Cryst. Growth Des. 11, 5507–5514. https://doi.org/10.1021/cg201163v.

Atuchin, V.V., Gavrilova, T.A., Kokh, K.A., Kuratieva, N.V., Pervukhina, N.V., Surovtsev, N.V., Tereshchenko, O.E., 2019. Structural and vibrational properties of PVT grown BiTeCl microcrystals. Mater. Res. Express 6, 045912. https://doi.org/10.1088/2053-1591/aafd45.

Audzijonis, A., Žaltauskas, R., Sereika, R., Žigas, L., Rėza, A., 2010. Electronic structure and optical properties of BiSI crystal. J. Phys. Chem. Solids 71, 884–891. https://doi.org/10.1016/j.jpcs.2010.03.042.

Dong, Z.L., Su, S.W., Zhang, Z.J., Jiang, Y., Xu, J.Y., 2023. NiFe-layered double hydroxides/lead-free $Cs_2AgBiBr$ 6 perovskite 2D/2D heterojunction for photocatalytic C_O2 conversion. Inorg. Chem. 62, 1752–1761. https://doi.org/10.1021/acs.inorgchem.2c04374.

Ganose, A.M., Butler, K.T., Walsh, A., Scanlon, D.O., 2016. Relativistic electronic structure and band alignment of BiSI and BiSeI: candidate photovoltaic materials. J. Mater. Chem. A 4, 2060–2068. https://doi.org/10.1039/C5TA09612J.

Ganose, A.M., Matsumoto, S., Buckeridge, J., Scanlon, D.O., 2018. Defect engineering of earth-abundant solar absorbers BiSI and BiSeI. Chem. Mater. 30, 3827–3835. https://doi.org/10.1021/acs.chemmater.8b01135.

Guo, M.J., Zhao, T.Y., Xing, Z.P., Qiu, Y.L., Pan, K., Li, Z.Z., Yang, S.L., Zhou, W., 2020. Hollow octahedral $Cu_{2-x}S$/CdS/Bi_2S_3 p-n-p type tandem heterojunctions for efficient photothermal effect and robust visible-light-driven photocatalytic performance. ACS Appl. Mater. Interfaces 12, 40328–40338. https://doi.org/10.1021/acsami.0c11360.

Huang, Y.H., Wang, K., Guo, T., Li, J., Wu, X.Y., Zhang, G.K., 2020. Construction of 2D/2D Bi_2Se_3/g-C_3N_4 nanocomposite with high interfacial charge separation and photo-heat conversion efficiency for selective photocatalytic CO_2 reduction. Appl. Catal. B: Environ. 277, 119232 https://doi.org/10.1016/j.apcatb.2020.119232.

Jatav, N., Kuntail, J., Khan, D., Kumar De, A., Sinha, I., 2021. AgI/$CuWO_4$ Z-scheme photocatalyst for the degradation of organic pollutants: experimental and molecular dynamics studies. J. Colloid Interface Sci. 599, 717–729. https://doi.org/10.1016/j.jcis.2021.04.120.

Ju, Y.J., Wang, Z., Lin, H.L., Hou, R.E., Li, H., Wang, Z., Zhi, R.T., Lu, X.Q., Tang, Y., Chen, F.J., 2024. Modulating the microenvironment of catalytic interface with functional groups for efficient photocatalytic degradation of persistent organic pollutants. Chem. Eng. J. 479, 147800 https://doi.org/10.1016/j.cej.2023.147800.

Khosroshahi, A.G., Mehrizad, A., 2019. Optimization, kinetics and thermodynamics of photocatalytic degradation of acid red 1 by Sm-doped CdS under visible light. J. Mol. Liq. 275, 629–637. https://doi.org/10.1016/j.molliq.2018.11.122.

Li, J., Huang, B.J., Guo, Q., Guo, S., Peng, Z.K., Liu, J., Tian, Q.Y., Yang, Y.E., Xu, Q., Liu, Z.Y., Liu, B., 2021. Van der Waals heterojunction for selective visible-light-driven photocatalytic CO_2 reduction. Appl. Catal. B: Environ. 284, 119733 https://doi.org/10.1016/j.apcatb.2020.119733.

Li, C.Y., Ma, Y., Zheng, S.Z., Hu, C.Y., Qin, F., Wei, L., Zhang, C.Q., Duo, S.W., Hu, Q.H., 2020. Acid etching followed by hydrothermal preparation of nanosized Bi_2O_4/Bi_2O_3 p-n junction as highly efficient visible-light photocatalyst for organic pollutants removal. J. Colloid Interface Sci. 576, 291–301. https://doi.org/10.1016/j.jcis.2020.02.115.

Li, L., Salvador, P.A., Rohrer, G.S., 2014. Photocatalysts with internal electric fields. Nanoscale 6, 24–42. https://doi.org/10.1039/C3NR03998F.

Li, X.R., Zhang, L., Niu, S., Dong, Z.J., Lyu, C., 2023. Quantitatively regulating the ketone structure of triazine-based covalent organic frameworks for efficient visible-light photocatalytic degradation of organic pollutants: Tunable performance and mechanisms. J. Hazard. Mater. 444, 130366 https://doi.org/10.1016/j.jhazmat.2022.130366.

Liu, D.D., Jiang, L.P., Chen, D.Q., Hao, Z.K., Deng, B.W., Sun, Y.Y., Liu, X., Jia, B.Y., Chen, L.M., Liu, H.T., 2024. Photocatalytic self-Fenton degradation of ciprofloxacin over S-scheme $CuFe_2O_4$/$ZnIn_2S_4$ heterojunction: mechanism insight, degradation pathways and DFT calculations. Chem. Eng. J. 482, 149165 https://doi.org/10.1016/j.cej.2024.149165.

Liu, J., Zhang, X.C., Zhong, Q., Li, J., Wu, H.Z., Zhang, B., Jin, L., Tao, H.B., Liu, B., 2020. Electrostatic self-assembly of a AgI/$Bi_2Ga_4O_9$ p-n junction photocatalyst for boosting superoxide radical generation. J. Mater. Chem. A 8, 4083–4090. https://doi.org/10.1039/C9TA13724F.

Liu, J., Wu, J., Wang, N.N., Tian, F.S., Li, J., 2022. Surface reconstruction of BiSI nanorods for superb photocatalytic Cr(VI) reduction under near-infrared light irradiation. Chem. Eng. J. 435, 135152 https://doi.org/10.1016/j.cej.2022.135152.

Liu, J., Zhang, Z.Z., Fan, Z., Tang, X.H., Zhong, Q., 2024. Strategies for boosting the photocatalytic reduction of toxic metal ions: progress and prospects. J. Water Process Eng. 57, 104683 https://doi.org/10.1016/j.jwpe.2023.104683.

Lu, N.L., Jing, X.D., Xu, Y., Lu, W., Liu, K.C., Zhang, Z.Y., 2023. Effective cascade modulation of charge-carrier kinetics in the well-designed multi-component nanofiber system for highly-efficient photocatalytic hydrogen generation. Acta Phys. Chim. Sin. 39, 2207045. https://doi.org/10.3866/pku.Whxb202207045.

Lu, N., Zhang, M.Y., Jing, X.D., Zhang, P., Zhu, Y.A., Zhang, Z.Y., 2022. Electrospun semiconductor-based nano-heterostructures for photocatalytic energy conversion and environmental remediation: opportunities and challenges. Energy Environ. Mater. 6, e12338.

Lu, N., Jing, X.D., Zhang, J.M., Zhang, P., Qiao, Q., Zhang, Z.Y., 2022. Photo-assisted self-assembly synthesis of all 2D-layered heterojunction photocatalysts with long-range spatial separation of charge-carriers toward photocatalytic redox reactions. Chem. Eng. J. 431, 134001 https://doi.org/10.1016/j.cej.2021.134001.

Lu, T.W., Zhang, R.B., Hu, C.Y., Chen, F., Duo, S.W., Hu, Q.H., 2013. TiO2-graphene composites with exposed 001 facets produced by a one-pot solvothermal approach for high performance photocatalyst. Phys. Chem. Chem. Phys. 15, 12963–12970. https://doi.org/10.1039/C3CP50942G.

Ma, Y.Y., Zhang, C.Q., Li, C.Y., Qin, F., Wei, L., Hu, C.Y., Hu, Q.H., Duo, S.W., 2019. Nanoscaled Bi_2O_4 confined in firework-shaped TiO_2 microspheres with enhanced visible light photocatalytic performance. Colloids Surf. A Physicochem. Eng. Asp. 580, 123757 https://doi.org/10.1016/j.colsurfa.2019.123757.

Ming, H.B., Wei, D.L., Yang, Y., Chen, B.Q., Yang, C., Zhang, J.S., Hou, Y.D., 2021. Photocatalytic activation of peroxymonosulfate by carbon quantum dots functionalized carbon nitride for efficient degradation of bisphenol A under visible-light irradiation. Chem. Eng. J. 424, 130296 https://doi.org/10.1016/j.cej.2021.130296.

Moroz, M.V., Prokhorenko, M.V., 2016. Phase equilibrium and thermodynamic properties of silver-saturated compounds BiSI and $Bi_{19}S_{27}I_3$ of the AgI-Bi-Bi_2S_3-BiSI system. Russ. J. Electrochem. 52, 392–395. https://doi.org/10.1134/S102319351604008X.

Podurets, A., Odegova, V., Cherkashina, K., Bulatov, A., Bobrysheva, N., Osmolowsky, M., Voznesenskiy, M., Osmolovskaya, O., 2022. The strategy for organic dye and antibiotic photocatalytic removal for water remediation in an example of Co-SnO_2 nanoparticles. J. Hazard. Mater. 436, 129035 https://doi.org/10.1016/j.jhazmat.2022.129035.

Quarta, D., Toso, S., Giannuzzi, R., Caliandro, R., Moliterni, A., Saleh, G., Capodilupo, A.-L., Debellis, D., Prato, M., Nobile, C., Maiorano, V., Infante, I., Gigli, G., Giannini, C., Manna, L., Giansante, C., 2022. Colloidal Bismuth Chalcohalide Nanocrystals 61, e202201747. https://doi.org/10.1002/anie.202201747.

Quarta, D., Toso, S., Saleh, G., Caliandro, R., Moliterni, A., Griesi, A., Divitini, G., Infante, I., Gigli, G., Giannini, C., Manna, L., Giansante, C., 2023. Mixed valence of bismuth in hexagonal chalcohalide nanocrystals. Chem. Mater. 35, 1029–1036. https://doi.org/10.1021/acs.chemmater.2c02941.

Ran, Z., Wang, X.J., Li, Y.W., Yang, D.W., Zhao, X.G., Biswas, K., Singh, D.J., Zhang, L.J., 2018. Bismuth and antimony-based oxyhalides and chalcohalides as potential optoelectronic materials, npj Comput. Mater. 4, 14. https://doi.org/10.1038/s41524-018-0071-1.

Salari, H., Kohantorabi, M., 2020. Facile template-free synthesis of new α-MnO_2 nanorod/silver iodide p-n junction nanocomposites with high photocatalytic performance. New J. Chem. 44, 7401–7411. https://doi.org/10.1039/D0NJ01033B.

Sudhir Ekande, O., Kumar, M., 2021. Facile synthesis of graphitic carbon nitride from acetic acid pretreatment to activate persulfate in presence of blue light for photocatalytic removal of metronidazole. Chemosphere 276, 130171. https://doi.org/10.1016/j.chemosphere.2021.130171.

Sun, H.P., Xiao, X.F., Celorrio, V., Guo, Z.F., Hu, Y., Kirk, C., Robertson, N., 2021. A novel method to synthesize BiSI uniformly coated with rGO by chemical bonding and its application as a supercapacitor electrode material. J. Mater. Chem. A 9, 15452–15461. https://doi.org/10.1039/D1TA02988F.

Tan, J.X., Chen, Z.Y., Chen, C.H., Hsieh, M.F., Lin, A.Y.C., Chen, S.S., Wu, K.C.W., 2023. Efficient adsorption and photocatalytic degradation of water emerging contaminants through nanoarchitectonics of pore sizes and optical properties of zirconium-based MOFs. J. Hazard. Mater. 451, 131113 https://doi.org/10.1016/j.jhazmat.2023.131113.

Wang, Z.Z., Jiang, L.S., Wang, K., Li, Y., Zhang, G.K., 2021. Novel AgI/$BiSbO_4$ heterojunction for efficient photocatalytic degradation of organic pollutants under visible light: Interfacial electron transfer pathway, DFT calculation and degradation mechanism study. J. Hazard. Mater. 410, 124948 https://doi.org/10.1016/j.jhazmat.2020.124948.

Wang, K., Li, Y., Zhang, G.K., Li, J., Wu, X.Y., 2019. 0D Bi nanodots/2D Bi_3NbO_7 nanosheets heterojunctions for efficient visible light photocatalytic degradation of antibiotics: Enhanced molecular oxygen activation and mechanism insight. Appl. Catal. B: Environ. 240, 39–49. https://doi.org/10.1016/j.apcatb.2018.08.063.

Wang, H.Y., Niu, R.R., Liu, J.H., Guo, S., Yang, Y.P., Liu, Z.Y., Li, J., 2022. Electrostatic self-assembly of 2D/2D $CoWO_4$/g-C_3N_4 p-n heterojunction for improved photocatalytic hydrogen evolution: built-in electric field modulated charge separation and mechanism unveiling. Nano Res. 15, 6987–6998. https://doi.org/10.1007/s12274-022-4329-z.

Wang, Q., Zheng, S.Z., Ma, W.G., Qian, J.Y., Huang, L.Y., Deng, H., Zhou, Q., Zheng, S.R., Li, S.J., Du, H., Li, Q., Hao, D., Yang, G.X., 2024. Facile synthesis of direct Z-scheme PPy/NH_2-UiO-66 heterojunction for enhanced photocatalytic Cr(VI) reduction, industrial electroplating wastewater treatment, and tetracycline degradation. Appl. Catal. B Environ. Energy 344, 123669. https://doi.org/10.1016/j.apcatb.2023.123669.

Wu, Y.Y., Hu, Y.X., Han, M.Q., Ouyang, Y.M., Xia, L.C., Huang, X.F., Hu, Z.F., Li, C.H., 2021. Mechanism insights into the facet-dependent photocatalytic degradation of perfluorooctanoic acid on BiOCl nanosheets. Chem. Eng. J. 425, 130672 https://doi.org/10.1016/j.cej.2021.130672.

Wu, S., Li, M., Xin, L., Long, H., Gao, X., 2022. Simultaneously photocatalytic removal of Cr(VI) and metronidazole by asynchronous cross-linked modified sodium alginate. J. Ind. Eng. Chem. 116, 339–350. https://doi.org/10.1016/j.jiec.2022.09.024.

Wu, Q., Song, Y.T., 2023. Enhanced interfacial charge migration through fabrication of p-n junction in $ZnIn_2S_4$/$NiFe_2O_4$/biochar composite for photocatalytic doxycycline

hydrochloride degradation. Chem. Eng. J. 453, 139745 https://doi.org/10.1016/j.cej.2022.139745.

Yang, R.F., Liang, B.P., Zheng, S.Z., Hu, C.Y., Xu, Y.J., Ma, Y.T., Bai, Y.Y., Dai, K.J., Tang, Y., Zhang, C.Q., Chang, M., 2022. Improving the surface oxygen vacancy concentration of Bi_2O_4 through the pretreatment of the $NaBiO_3{\cdot}2H_2O$ precursor as a high-performance visible light photocatalyst. Inorg. Chem. 61, 14102–14114. https://doi.org/10.1021/acs.inorgchem.2c02163.

Yuan, Q., Huang, J.D., Li, A., Lu, N., Lu, W., Zhu, Y.A., Zhang, Z.Y., 2024. Engineering semi-reversed quantum well photocatalysts for highly-efficient solar-to-fuels conversion. Adv. Mater. 36, 2311764. https://doi.org/10.1002/adma.202311764.

X.K. Zhang, J. Liu, H.Z. Zhang, Z. Wan, J. Li, Uncovering the pathway of peroxymonosulfate activation over $Co_{0.5}Zn_{0.5}O$ nanosheets for singlet oxygen generation: Performance and membrane application, Appl. Catal. B: Environ., 327 (2023) 122429, Doi: 10.1016/j.apcatb.2023.122429.

Zhang, L.L., Hu, C., Ji, H.H., 2017. p-AgI anchored on 001 facets of n-Bi2O2CO3 sheets with enhanced photocatalytic activity and stability. Appl. Catal. B: Environ. 205, 34–41. https://doi.org/10.1016/j.apcatb.2016.12.015.

Zhang, Z.Q., Liang, J.L., Zhang, W., Zhou, M., Zhu, X.L., Liu, Z.Y., Li, Y., Guan, Z.Q., Lee, C.-S., Wong, P.K., Li, H.M., Jiang, Z.F., 2023. Modified-pollen confined hybrid system: a promising union for visible-light-driven photocatalytic antibiotic degradation. Appl. Catal. B: Environ. 330, 122621 https://doi.org/10.1016/j.apcatb.2023.122621.

Zhang, X.D., Yan, J., Zheng, F.Y., Zhao, J., Lee, L.Y.S., 2021. Designing charge transfer route at the interface between WP nanoparticle and g-C_3N_4 for highly enhanced photocatalytic CO_2 reduction reaction. Appl. Catal. B: Environ. 286, 119879 https://doi.org/10.1016/j.apcatb.2021.119879.

Zhang, M.J., Zhang, Y., Zhu, Y., Wang, J.J., Qiao, L., Zhao, Y., Tao, Y., Xiao, Y., Tang, L., 2023. Insights into adsorption and high photocatalytic oxidation of ciprofloxacin under visible light by intra-molecular Donor-Acceptor like p-n isotype heterojunction: performance and mechanism. Chem. Eng. J. 464, 142533 https://doi.org/10.1016/j.cej.2023.142533.

Zhao, W., Li, J., Dai, B.L., Cheng, Z.P., Xu, J.M., Ma, K.R., Zhang, L.L., Sheng, N., Mao, G. X., Wu, H.W., Wei, K.X., Leung, D.Y.C., 2019. Simultaneous removal of tetracycline and Cr(VI) by a novel three-dimensional AgI/$BiVO_4$ p-n junction photocatalyst and insight into the photocatalytic mechanism. Chem. Eng. J. 369, 716–725. https://doi.org/10.1016/j.cej.2019.03.115.

Zheng, S.Z., Zhang, C.Q., Ma, Y.T., Yang, R.F., Qin, F., Wei, L., Hu, C.Y., 2021. Hierarchical polypyrrole encapsulating Bi_2O_4 to enhance charge separation and light absorption with boosted visible light photocatalytic activity. Ceram. Int. 47, 10574–10581. https://doi.org/10.1016/j.ceramint.2020.12.169.

Zheng, S.Z., Qin, F., Hu, C.Y., Zhang, C.Q., Ma, Y.T., Yang, R.F., Wei, L., Bao, L.W., 2021. Up-converted nitrogen-doped carbon quantum dots to accelerate charge transfer of dibismuth tetraoxide for enhanced full-spectrum photocatalytic activity. Colloids Surf. A Physicochem. Eng. Asp. 615, 126217 https://doi.org/10.1016/j.colsurfa.2021.126217.

Zhong, Q., Liu, J., Wang, Z.Z., Ghasemi, J.B., Zhang, G.K., 2021. Ti_3C_2 MXene/Ag_2ZnGeO_4 Schottky heterojunctions with enhanced photocatalytic performances: efficient charge separation and mechanism studies. Sep. Purif. Technol. 278, 119560 https://doi.org/10.1016/j.seppur.2021.119560.

Zhou, J.X., Tang, H.L., Yao, C.X., Song, W.G., Liu, C.B., Song, W., Zhang, Z.J., 2024. 2D/2D Ni-MOF/BiOCl S-scheme heterojunction with boosted charge transfer and photocatalytic degradation of tetracycline. Sustain. Mater. Techno. 39, e00825.

Zhou, C.X., Wang, R.L., Jiang, C.P., Chen, J.W., Wang, G., 2019. Dynamically optimized multi-interface novel BiSI-promoted redox sites spatially separated n-p-n double heterojunctions BiSI/MoS_2/CdS for hydrogen evolution. Ind. Eng. Chem. Res. 58, 7844–7856. https://doi.org/10.1021/acs.iecr.9b00234.

Zhou, Z.Y., Zhang, L.G., Su, W.A., Li, Y., Zhang, G.K., 2021. Facile fabrication of AgI/Sb_2O_3 heterojunction photocatalyst with enhanced visible-light driven photocatalytic performance for efficient degradation of organic pollutants in water. Environ. Res. 197, 111143 https://doi.org/10.1016/j.envres.2021.111143.